J Nanopart Res (2020) 22: 66
https://doi.org/10.1007/s11051-020-4758-0

REVIEW

High-moment magnetic nanoparticles

Jinming Liu · Diqing Su · Kai Wu · Jian-Ping Wang

Received: 18 September 2019 / Accepted: 16 January 2020 / Published online: 3 March 2020

Abstract In recent years, high-moment magnetic nanoparticles (MNPs) such as FeCo are attracting intense interest for biomedical applications. The synthesized FeCo MNPs have the specific saturation magnetization up to 226 emu/g that is more than three times higher than that of iron oxide MNPs (~ 70–80 emu/g). Core-shell MNPs are also synthesized to enhance the functionality of high-moment MNPs. Shells like SiO_2, Au, and Ag are used for these high-moment MNPs to improve biocompatibility. The sputtering-based gas-phase condensation approach to synthesize high-moment MNPs and core-shell nanostructures are reviewed. The applications of these high-moment MNPs such as magnetic hyperthermia, drug delivery, magnetic resonance imaging (MRI), and biosensing are summarized. The heating efficiency of magnetic hyperthermia and drug delivery could be significantly enhanced by using high-moment MNPs. MNPs with different crystallinity and shapes (such as cubic, spherical, triangular, and octahedral shapes) are also summarized due to their potential applications in MRI. High-moment MNPs could also provide more magnetic signals for giant magnetoresistance (GMR)-based biosensors, which are also reviewed. We believe that the high-moment MNPs are promising candidates for many bio-applications.

Keywords High-moment · Magnetic nanoparticles · Gas-phase condensation · FeCo · Bio-application · Biocompatible nanoshells

Introduction

Magnetic nanoparticles (MNPs) are attracting increasing attention due to their wide applications such as magnetic hyperthermia, drug delivery, magnetic resonance imaging (MRI), magnetic biosensing, etc., as shown in Fig. 1 (Kline et al. 2009; Li et al. 2009; Patra et al. 2010; Jing et al. 2015; Krishna et al. 2018; Wu et al. 2019b). These applications mainly rely on magnetic signals generated by MNPs. Therefore, high-moment MNPs are preferred to iron oxide MNPs since they can provide stronger magnetic signals while

This article is part of the topical collection *Nanoparticles in Biotechnology and Medicine*

Xiaoshan (Sean) Zhu, University of Nevada, Guest Editor

J. Liu · K. Wu · J.-P. Wang (✉)
Department of Electrical and Computer Engineering, University of Minnesota, Minneapolis, MN 55455, USA
e-mail: jpwang@umn.edu

D. Su
Department of Chemical Engineering and Material Science, University of Minnesota, Minneapolis, MN 55455, USA

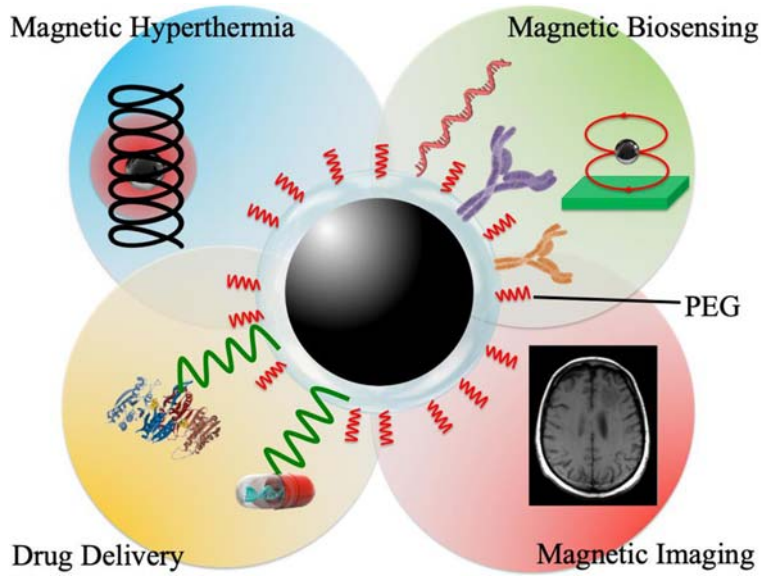

Fig. 1 Schematic representation of multifunctional MNPs, polyethylene glycol (PEG) coatings are used to improve solubility and decrease immunogenicity. (MRI reprinted with permission from Serkova (2017) copyright 2017, under the terms of the Creative Commons Attribution License (CC BY))

maintaining a small size. As a result, high-moment MNPs can provide enough signal with a relatively low dose and high signal-to-noise ratio. Nowadays, iron oxide MNPs such as γ-Fe_2O_3 and Fe_3O_4 are widely used in the applications aforementioned since they are stable and biocompatible (Jing et al. 2013). However, one drawback of iron oxide MNPs is that their saturation magnetizations (M_s) are relatively low compared to the high saturation magnetization materials such as Fe and FeCo alloys (Jing et al. 2009; Liu et al. 2016; Liu et al. 2018). As a result, larger iron oxide MNPs are needed to provide stronger magnetic signals, like using iron oxide microbeads. However, they inevitably encounter physical limitations for some applications that require relatively small size and superparamagnetic MNPs. For example, in the in vivo applications like MRI and drug delivery, the MNPs should be small enough to transport in blood circulation systems and interact with cells (Zhang et al. 2008; Bárcena et al. 2009). In vitro biomarker detection applications usually require MNPs the size of proteins (15–20 nm) (Srinivasan et al. 2009a). Thus, it is more practical to enhance the magnetic signal by using MNPs with high M_s rather than increasing their size. MNPs with high M_s (high-moment MNPs) such as Fe, Co, and FeCo alloys are preferred for bioapplications.

Great efforts have been made to fabricate high-moment MNPs. However, it is still challenging to make these MNPs with well-controlled properties. Physical methods such as arc plasma and pulsed laser deposition are used to prepare the MNPs, but the fabricated MNPs show irregular shapes and poor crystallinity (Ong et al. 2008; Bulut et al. 2009). Although some MNPs like iron oxide are well synthesized by wet chemical methods, it is still challenging to make iron-based high-moment MNPs with controlled phase and crystallinity due to the formation of intermediate complexes and relatively low reaction temperature (Wei et al. 2008).

During the past decades, researchers have made great efforts to prepare MNPs using a gas-phase condensation (GPC) method. Granqvist and Buhrman synthesized ultrafine particles using a GPC method in the 1970s (Granqvist 1976). Instead of using a sputtering source, a thermal evaporation source was applied, and particles were formed in static, inert gas. The size and crystallinity of the nanoparticles, however, were uncontrollable. The following work was to solve those two issues. Later a pressure differential was introduced into a GPC system, and synthesized nanoparticles followed the gas flow to be collected on a substrate (Sattler et al. 1980). A skimmer was put into the system to select these synthesized nanoparticles, and nanoparticles with a narrower size distribution were obtained. In 1991, sputtering sources with planar targets were used in the GPC system, and varieties of materials could be used for preparing nanoparticles (Haberland et al. 1991, 1992). Sugimoto pointed out that the key to making nanoparticles with narrow size distribution was to separate the

nucleation and growth of nanoparticles (Sugimoto 1987). In this way, each nanoparticle had similar growth time, and the size of them was close. Based on this proposal, Yamamuro et al. obtained monodispersed Cr nanoparticles (Yamamuro et al. 1998, 1999). Thus, nanoparticles with narrow size distribution were achieved. However, the control of the crystallinity of particles was still challenging at that time.

In 2005, Wang's group reported that a field-controlled plasma heating effect in a sputtering-based GPC system could help control the crystallinity and phase separation of nanoparticles (Bai and Wang 2005; Qiu and Wang 2007; Xu and Wang 2008; Jing et al. 2013, 2015; Liu et al. 2018). Different kinds of monodispersed MNPs with controlled phase and crystallinity were successfully made, such as $L1_0$-FePt, FeCo, $SmCo_5$, body-centered tetragonal Fe MNPs, etc.(Qiu et al. 2005; Xu 2007; He et al. 2013; Liu et al. 2018, 2020b).

One concern of these high-moment MNPs like FeCo is the potential toxicity for in vivo bio-applications. One of the solutions is to synthesize core-shell nanoparticles. MNPs with high M_s act as the core and biocompatible materials such as Au, Ag, SiO_2, etc. and serve as the shells (Bai and Wang 2005; Bai et al. 2007a). In this way, the core-shell nanoparticles have both high magnetic moment and biocompatibility.

In this review, the research of high-moment MNPs and core-shell nanoparticles made by a GPC method is introduced, and the mechanism and challenges of synthesizing them are summarized. We will mainly focus on the merit of using high-moment MNPs in bio-applications such as magnetic hyperthermia, drug delivery, magnetic resonance imaging (MRI), and magnetic biosensors.

The working mechanism of the GPC system

Figure 2 shows the schematic drawing of the GPC system used for synthesizing different MNPs. There are two chambers separated by the orifices. The left is the sputtering chamber, where the nucleation and growth of MNPs take place. The right is the deposition chamber, where the MNPs are collected on a substrate. In the sputtering chamber, a DC magnetron sputtering source is used to provide atoms for the nucleation and growth of MNPs. The sputtering source is horizontally movable to tune the volume of the sputtering chamber. The sputtering chamber is double-walled and cooled by water (~10 °C). The sputtering gas pressure is around several hundreds of mTorr during the fabrication of MNPs. The high sputtering pressure helps the sputtered atoms to cool down quickly, and then the nucleation and growth begin for MNPs. Meanwhile, there is a pump placed in the deposition chamber to create a pressure difference between these two chambers. Due to this pressure difference ($P_1 >> P_2$), the MNPs are formed in the sputtering chamber flow along with the sputtering gas into the deposition chamber and are collected by a substrate, as shown in Fig. 2. In addition, a carrier gas-like argon could also be inducted into the sputtering chamber to adjust the gas velocity in the sputtering chamber and tune the nucleation and growth processes of the MNPs (Jian-Ping 2008).

The nucleation and growth of the MNPs happen near the target surface. Thus, the intensity and distribution of the magnetic field near the target surface play a significant role in the morphology and crystallinity of synthesized MNPs. For a planar target of a magnetron sputtering source, an etching groove is formed during the sputtering process. When preparing thin film samples, the nucleation and growth of these sputtered atoms start on a substrate that is far away from the sputtering source. So, the magnetic field intensity near the etching grove of a sputtering target has little effect on the morphology and crystallinity of thin films. However, the depth of the etching groove is crucial to the structure and morphology of these synthesized MNPs since the nucleation and growth of MNPs happen near the surface of the sputtering target (~ several mm near the target surface). In addition, the magnetic planar targets used for preparing MNPs usually have high magnetic permeability, and the magnetic flux is mostly confined in the target. Only a small portion of the magnetic flux escapes from the target and helps generate the plasma during the sputtering process. Thus, the depth of the etching groove in a magnetic target has a significant influence on the intensity and distribution of magnetic fields and on the nucleation and growth of MNPs.

MNPs prepared by a new magnetic target without an etching groove show a uniform size distribution. When the target is sputtered for a while, there is a deep etching groove in the target, and larger MNPs are obtained with nonuniform size distribution. The plasma density for a target with a deep etching groove is higher due to the enhanced magnetic field at the etching groove compared to that of a new target. Thus, the plasma density may

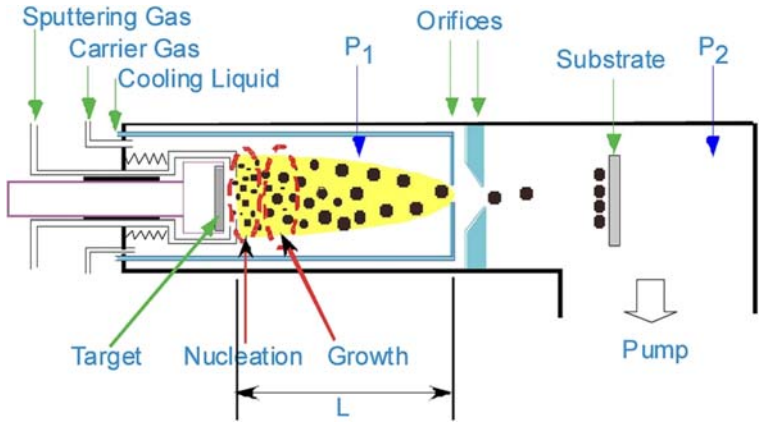

Fig. 2 Schematic drawing of the GPC system for synthesizing MNPs. A pressure difference is created between the sputtering chamber (left) and the deposition chamber (right). P_1 (several hundred mTorr) is much higher than that of P_2. MNPs are formed in the sputtering chamber and collected from the substrate placed in the deposition chamber (Reprinted with permission from Jian-Ping (2008), copyright 2008 IEEE)

provide a way to manipulate the thermal environment when synthesizing MNPs.

Two possible models are proposed for the growth of MNPs prepared by a GPC system based on the overlap between the growth zone of MNPs and the plasma zone. In the first model, the nucleation and growth of MNPs happen in the plasma region (the hot region). Then the MNPs are cooled down when they fly away from the hot region and conserve the high-temperature phase. In this model, the MNPs show good crystallinity with a relatively large size. In the second model, the nucleation and growth zone of MNPs are partially overlapped with the plasma zone. Thus, the sputtered atoms are cooled down quickly since they fly into the cold region (away from the plasma region) during the nucleation and growth process. Therefore, the temperature of the sputtered atoms decreases rapidly, and high supersaturation of the sputtered atoms is obtained. The nucleation rate is very high, and relatively small MNPs are obtained but with poor crystallinity.

Based on these possible models, a soft iron ring and cone are placed on top of a planar target to obtain MNPs with good crystallinity, as shown in Fig. 3. Since soft iron has high magnetic permeability, the ring and cone enhance the magnetic flux intensity at the surface of the target and also extend the plasma region to widen the hot zone. In this case, the first model mentioned above happens, and MNPs with good crystallinity are synthesized (Qiu and Wang 2006).

Synthesis of high-moment MNPs

High-moment magnetic materials such as Fe, FeCo, and $Fe_{16}N_2$ are attracting attention (Xu et al. 2007; Liu et al. 2018, 2019b, 2020a; Wang 2019). MNPs fabricated by these high-moment magnetic materials have much higher magnetic signals compared to iron oxide MNPs like γ-Fe_2O_3 and Fe_3O_4. The magnetization of superparamagnetic Fe_3O_4, FeCo, and $Fe_{16}N_2$ at different applied fields are shown in Table 1. High-moment FeCo and $Fe_{16}N_2$ MNPs show much higher moment at all the field range than that of Fe_3O_4. Here, the synthesis of FeCo MNPs is used as an example. FeCo MNPs with a specific saturation magnetization up to 226 emu/g were synthesized using a GPC method (Xu et al. 2007). A Fe_xCo_{100-x} planar target is used to synthesize these FeCo MNPs using the GPC method. The thickness of the target is around 1 mm that helps obtain enough magnetic flux intensity at the target surface to generate magnetron plasma. A soft iron ring and cone are placed at the surface of the FeCo alloy target to tune the intensity and distribution of magnetic fields near the target surface. Copper disks are placed under the planar FeCo alloy target to adjust the magnetic flux intensity, as shown in Fig. 2. Thus, the nucleation and growth could be adjusted to either model one (bigger size with good crystallinity) or model two (smaller size with poor crystallinity) discussed in Sect. 2.

The shape of the MNPs synthesized by the GPC method can also be adjusted. Cubic and spherical FeCo MNPs with a narrow size distribution are synthesized by the GPC method (Xu et al. 2007). These MNPs with different shapes show quite different magnetic properties and can be utilized in various applications such as MRI. As discussed in Sect. 2, surface magnetic field distribution (SMFD) of the target surface has a significant influence on the structure and morphology of MNPs. In order to characterize the SMFD, a parameter d_{700} is used to indicate the difference, where d_{700} is

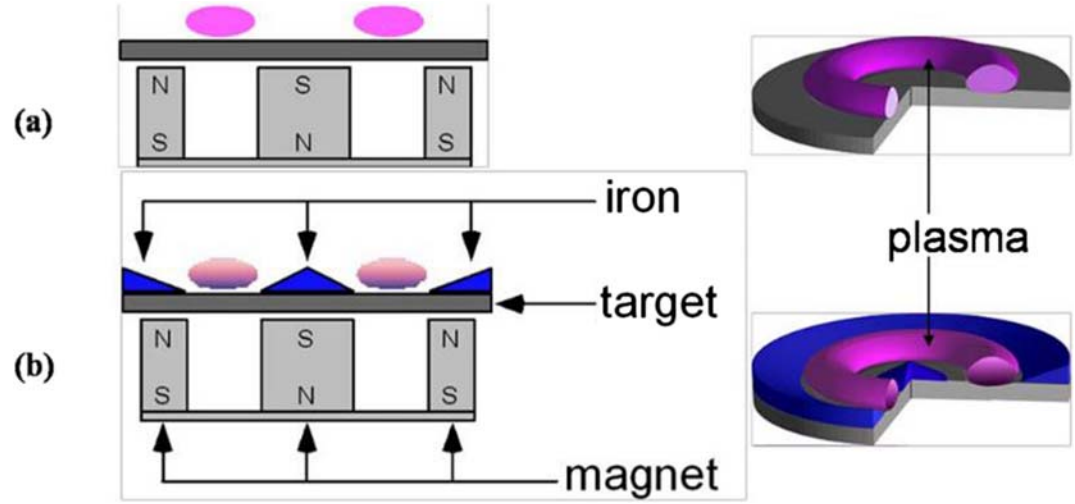

Fig. 3 Schematic drawing of a traditional planar target, which leads to the MNPs growth model two (reprinted with permission from Qiu and Wang et al. (2006), copyright 2006 American Institute of Physics)

defined as the distance from the surface of the target with 700 Oe field parallel to the target surface. The smaller the value of d_{700}, the larger the intensity of the surface magnetic field of the target. When d_{700} is 6.5 mm, cubic FeCo MNPs are obtained, and only body-centered cubic (bcc) FeCo structure is detected based on the transmission electron microscope (TEM) diffraction results. When d_{700} is increased to 8.5 mm, spherical FeCo MNPs are obtained. Several structures of these FeCo MNPs such as bcc, face-centered cubic (fcc), and hexagonal close-packed (hcp) are detected by TEM diffraction patterns. A higher magnetic field at the surface of the target induces a larger d_{700}. The high magnetic field at the target surface will enhance the plasma intensity, and the effective temperature near the target surface could also be increased. Thus, a high-temperature phase is obtained for FeCo MNPs (Bai et al. 2007b). FeCo MNPs with other shapes such as octahedron and truncated octahedron have also been made. MNPs of different shapes show different effects on a local magnetic field, which could be used to enhance the contrast in MRI and tag different species (Xu et al. 2007).

$Fe_{1-x}Co_x$ MNPs synthesized by the GPC method have different sizes ranging from 3 to 100 nm. The specific saturation magnetization of these FeCo MNPs is up to 226 emu/g, which is much higher than that of iron oxide MNPs (~ 70–80 emu/g) (Jing et al. 2009, 2013). Hysteresis loops are characterized on FeCo MNPs. For well-dispersed FeCo MNPs, they are superparamagnetic when the size of the MNPs is below the superparamagnetic critical size. The X-ray diffraction pattern (XRD) and hysteresis loops of well-dispersed FeCo MNPs are characterized, as shown in Fig. 4. The XRD pattern indicates that FeCo MNPs have bcc structure. The specific saturation magnetization of FeCo MNPs varies with the Fe/Co ratio, but it is around 200 emu/g, which is still much higher than that of iron oxide MNPs. However, large coercivity and remanence of the FeCo MNPs are observed when they aggregate

Table 1 The magnetizations (M) of three superparamagnetic MNPs are given at different applied magnetic fields.

Magnetic field (Oe)	M (emu/cm^3) Fe_3O_4	M (emu/cm^3) FeCo	M (emu/cm^3) $Fe_{16}N_2$
10	0.45	2.04	2.54
50	2.27	10.23	12.72
100	4.53	20.45	25.43
500	22.62	102.09	126.92
1000	45.00	203.07	252.46

The size of these three MNPs is set to 4 nm. The hysteresis loops of these MNPs are calculated using the Langevin function

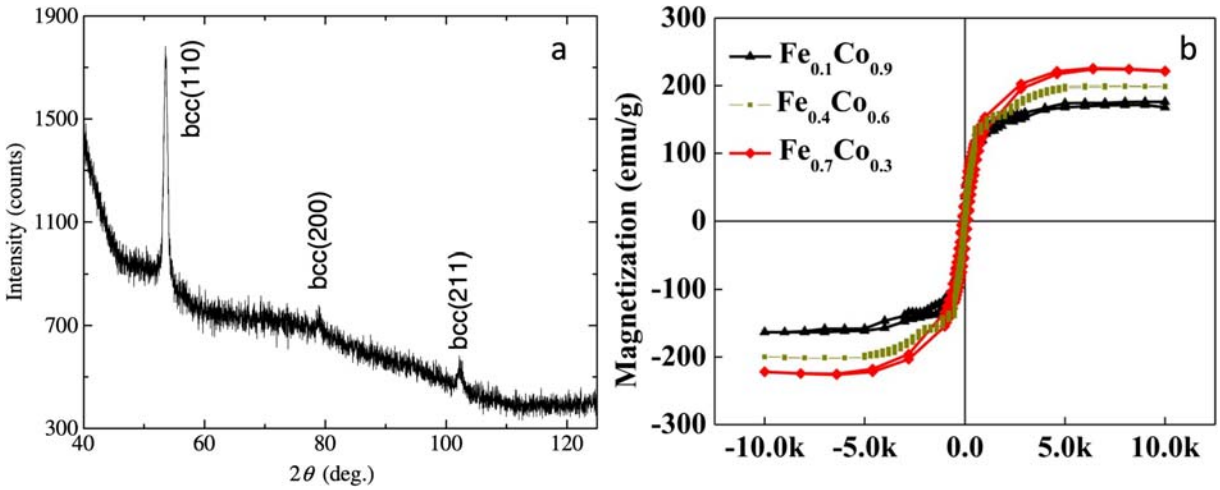

Fig. 4 **a** X-ray diffraction patterns of $Fe_{0.6}Co_{0.4}$ nanoparticles. **b** Hysteresis loops of $Fe_{1-x}Co_x$ ($x = 0.3, 0.6, 0.9$) MNPs (reprinted with permission from Bai et al. (2007a) and Jing et al. (2013), copyright 2007 IOP, 2013 IEEE)

together or form a chain structure (Liu et al. 2016). For applications requiring superparamagnetic nanoparticles, the MNPs should be well-dispersed. There are several bio-applications based on the high-moment MNPs, which will be summarized in the following sections. Besides FeCo, other MNPs such as Fe, Co, and FeSi are also fabricated using this GPC method (Xu and Wang 2008; Jing et al. 2015; Liu et al. 2018).

In addition, a hollow cathode is also developed for the GPC system that could significantly enhance the yield of MNPs. Compared to the GPC system with a planar target, the yield of FeCo MNPs synthesized by the GPC system with the hollow cathode is four times higher. Meanwhile, the target utilization rate of the hollow source is around 18 times higher than that of the planar target. Thus, this new design could significantly enhance the yield of high-moment FeCo MNPs synthesized by the GPC method (Liu et al. 2019a).

The subsequent surface functionalization of the synthesized high-moment MNPs can be done directly by depositing these MNPs onto a polymer-coated glass substrate. As reported by Wang et al., the $L1_0$ phase FePt MNPs are directly deposited onto poly(vinyl alcohol) (PVA)-coated glass substrate to prevent the agglomeration of MNPs (see Fig. 5) (Wang et al. 2006). Then the MNPs are collected in a vial containing water, PEG-SH, and PEG-COOH ligands. The vial is stirred on a shaker for 3 h followed by sonication, and then the excess polymer matrix/ligands are removed by centrifugation. By adjusting the molecular weight of the PEG segment, the interparticle distance can be easily adjusted.

Synthesis of high-moment MNPs with core-shell structures

Although high-moment MNPs like FeCo can provide much higher magnetic signals than that of iron oxide MNPs, one big concern of these high-moment MNPs is their toxicity that may hinder their bio-applications. One solution is to coat a biocompatible shell on high-moment MNPs to form core-shell MNPs. Different shell materials such as Au, Ag, and SiO_2 have been used to synthesize the core-shell MNPs directly by the GPC method (Bai et al. 2007a).

Two approaches have been applied to synthesize the core-shell MNPs by the GPC method. In the first approach, the MNPs are made by a sputtering source and online sputtering sources or evaporation sources that are put in the deposition chamber to coat these synthesized MNPs with biocompatible shells like Au and Ag as shown in Fig. 6 (Bai and Wang 2005). This approach could prepare various kinds of core-shell structures with different MNP cores and shells.

The second approach is to form core-shell structures directly based on different surface and strain energies of the core and the shell materials. Taking FeCo@Au MNPs as an example, a FeCo and Au composite target is used (Xu et al. 2007) to synthesize FeCo@Au MNPs. Higher sputtering pressure is applied to make sure FeCo and Au are quickly solidified. The gas flow rate is tuned to provide enough time for the diffusion of these Fe, Co, and Au elements. Au has lower surface energy than that of Fe and Co, and it will diffuse to the surface of

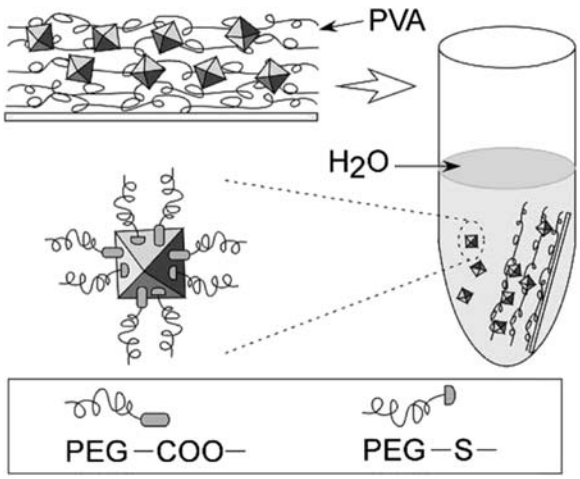

Fig. 5 Solubilization of $L1_0$ FePt nanoparticles into aqueous solution. Particles are deposited onto poly(vinyl alcohol) (PVA) coated a substrate with an appropriate amount of poly(ethylene glycol) (PEG)-based ligands (PEG-SH, PEG-COOH) added. Then, the substrate is immersed in a vial containing the above ligands aqueous solution. Stirred with a shaker then followed by sonication, these particles become soluble in water and stable (reprinted with permission from Wang et al. (2006), copyright 2006 IEEE)

nanoparticles to form a gold shell when the diffusion time is long enough. Thus, the experimental parameters like the sputtering pressure, gas flow, etc. are tuned to obtain a low rate of solidification, and there is a sufficient diffusion time for Au to form the Au shell. As shown in Fig. 7 a and b, the converged beam electron diffraction (CBED) technique is used to study the crystal structure of the fabricated FeCo@Au nanoparticles. The composition distribution of a cross section is obtained at a single FeCo@Au particle level by using the energy dispersive X-ray spectroscopy and plotted in Fig. 7 c with the measured particle shown in the inset. It indicates that there are more Au atoms at the surface of the FeCo@Au particle than in the core, and the opposite is true for Fe and Co, which is a significant sign of FeCo core and Au shell structure.

Bio application of high-moment MNPs

MNPs with high saturation magnetizations are attracting wide attention due to their advanced magnetic properties in hyperthermia therapy, drug delivery, imaging, and biosensing applications. For example, high-moment MNPs are pursued in the areas of hyperthermia and drug delivery for their easy manipulation through an external magnetic field, in the magnetic resonance imaging (MRI) for a better contrast, in biosensing applications for a higher sensor signal and sensitivity. In this section, we reviewed some recent works on applying high-

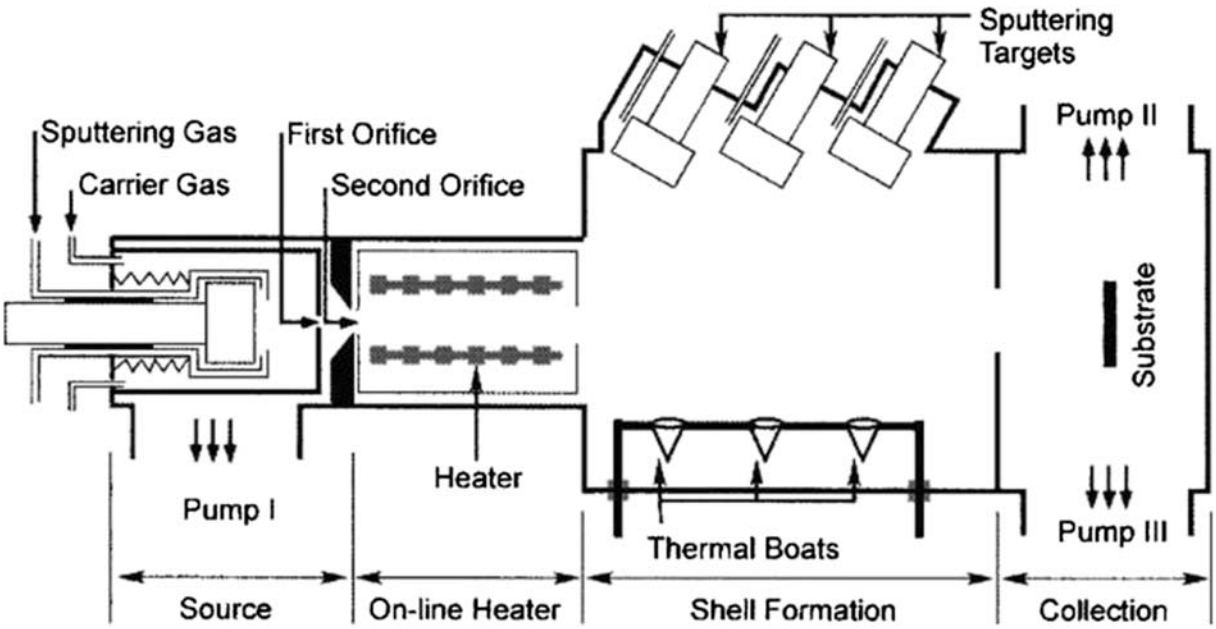

Fig. 6 Schematic configuration of the GPC system used for preparing core-shell nanoparticles. The left source is used to prepare MNPs, and the thermal boats and sputtering targets are for the shell of the MNPs (reprinted with permission from Bai and Wang (2005), copyright 2005 American Institute of Physics)

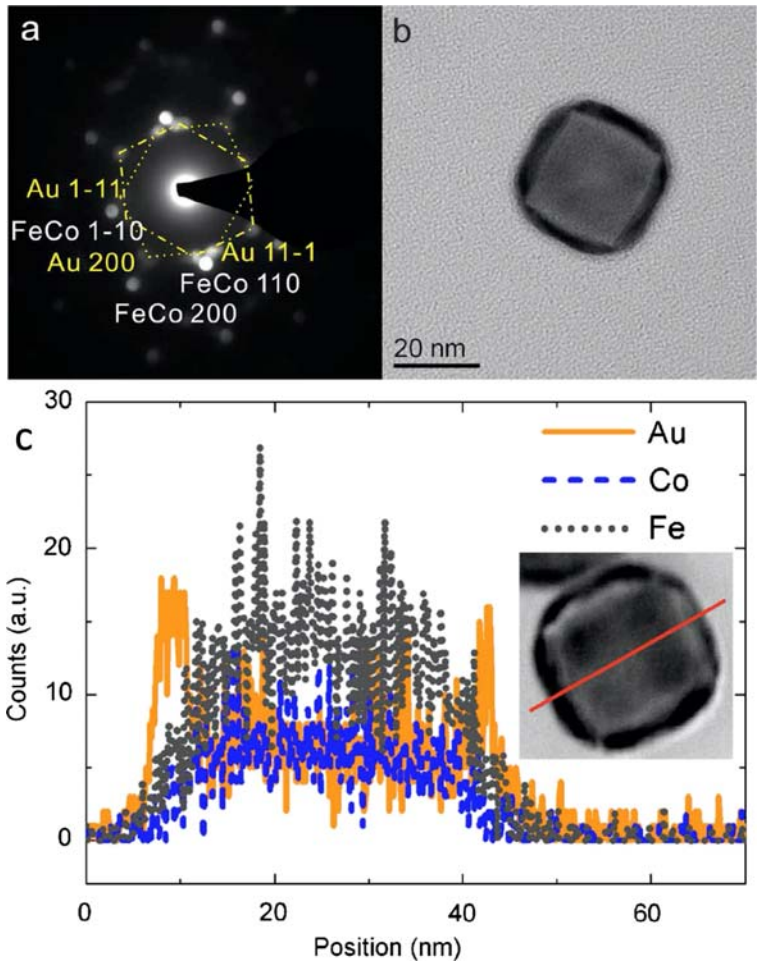

Fig. 7 Structures of FeCo@Au nanoparticle. **a** The converged beam electron diffraction (CBED) of the nanoparticle in **(b)**, the two distorted hexagons (dot line and dash-dot line) indicate two perpendicular Au [011]s. **b** A TEM bright-field image of a single FeCo@Au nanoparticle. **c** Composition distribution of a cross section of a single FeCo@Au nanoparticle. The single nanoparticle is shown in the inset. The line in the insert indicates the path of the electron beam (reprinted with permission from Xu and Wang (2007), copyright 2007 American Institute of Physics)

moment MNPs in magnetic hyperthermia, drug delivery, MRI, and magnetic biosensing.

Magnetic hyperthermia

In the area of magnetic hyperthermia therapy, MNPs act as tiny heating sources when exposed to an alternating magnetic field (Wu and Wang 2017). Many recent studies have focused on using iron oxide nanoparticles as heating elements due to t he known biocompatibility and commercial availability (Bañobre-López et al. 2013; Yu et al. 2014; Wu and Wang 2017; Hedayatnasab et al. 2017). However, the major drawback of iron oxide MNPs is the relatively low-specific saturation magnetizations.

Theoretically, the specific loss power is proportional to the square of the magnetic moment. High-moment MNPs are preferred in order to maximize the heating efficiency and to lower the thermal dose delivered to tumor regions. Kline et al. (2009) proposed the FeCo@Au core-shell heterostructure nanoparticles could be used for magnetic hyperthermia and demonstrated the feasibility of using FeCo@Au as tiny heating agents. FeCo@Au nanoparticles were synthesized using a sputtering-based GPC technique, and uniform size distribution of these MNPs was also achieved (Xu and Wang 2008; Liu et al. 2016).

The heating efficiency of FeCo@Au nanoparticles can be further tuned by adjusting the mean size and size distribution of these nanoparticles, and the AC magnetic field. Lacroix et al. (2009) reported the hyperthermia measurements on a colloidal solution of single-domain, monodispersed FeCo MNPs and carried out the theoretical studies on the frequency-dependent hysteresis shapes of noninteracting nanoparticles. Although the saturation magnetization of these fabricated FeCo nanoparticles is below the bulk FeCo alloy, they achieved a measured losses of 1.5 mJ/g that is comparable to the highest value of the literature (1.5 mJ/g for iron oxide nanoparticles (Hergt et al. 2004) and 1.25 mJ/g and 1.75 mJ/g for Co nanoparticles (Zeisberger et al. 2007)). More recently, Celik et al. reported the synthesis of FeCo MNPs with well-controlled size in the range of 11.5–37.2 nm by the surfactant-assisted ball milling method. They achieved a specific absorption rate (SAR) of 2–15 W/g for a magnetic field with the frequency of 171 kHz and the field strength between 6 and 14 mT (Çelik and Fırat 2018).

Drug delivery using high-moment MNPs

MNPs working as therapeutic drug carriers are proposed in the 1970s to target on a specific site (Dobson 2006). MNPs could combine drugs with a thermally sensitive polymer to carry out the drug delivery. Once MNPs with drugs arrive at a specific location, an ac magnetic field is applied to stimulate MNPs to generate heat to decompose the thermally sensitive polymer and release the drugs (Jing et al. 2015). The challenge is how to monitor the temperature of the MNPs lively to make sure MNPs are not overheated. The temperature may be monitored for in vitro cases, but for in vivo cases, it is difficult to do so (Jing et al. 2015). Jing et al. demonstrated that Fe-Si MNPs have intrinsically tunable heat generation capability by doping Si into Fe MNPs. Si atoms can reduce the exchange interaction between Fe atoms and decrease the Curie temperature of Fe MNPs accordingly. When the temperature of MNPs is close to their Curie temperature, these MNPs will automatically stop heating since they magnetically transform from a ferromagnet to a paramagnet. In this way, the stop-heating temperature of Fe-Si MNPs could be tuned by controlling the content of Si in these MNPs. Additionally, Fe-Si MNPs show good biocompatibility that is crucial for bio-applications.

In their work, a GPC method was used to fabricate the Fe-Si NPs with wide Si content and various Curie temperatures (Jing et al. 2015). Figure 8 a shows the TEM bright-field image of cubic Fe-Si nanoparticles composed of 38% Si, and Fig. 8 b shows the respective selected area diffraction (SAD) pattern. These results demonstrate that the fabricated Fe-Si nanoparticles are highly crystalline and these nanoparticles have an hcp structure. The cytotoxicity of Fe-Si nanoparticles is also investigated by testing in cultured mouse embryonic fibroblasts (NIH 3 T3) and human umbilical vein endothelial cells (HUVECs) as shown in Fig. 8 c and d. Compared to other metallic nanoparticles (Hu et al. 2008; Xu et al. 2009), Fe-Si shows low toxicity. The performance and the ability for drug delivery of these nanoparticles are investigated in Fig. 8 e–h, where the temperature change of the composite during magnetic field heating is recorded in Fig. 8 i. These Fe-Si nanoparticles are incorporated in a thermosensitive copolymer poly(ortho ester amides) (POEA). A composite sample is prepared by incorporating the Fe-Si nanoparticles with a Fluorescein Rhodamine B dye into the POEA gel, which is used to demonstrate the drug release. Figure 8 e and g show the images of composite samples with and without Fe-Si MNPs respectively before turning on the ac magentic field. The temperutre of these samples are 37 ^{o}C . After turning on the ac magentic field, the color cchanges as shown in Fig. 8 f (with Fe-Si MNPs) and Fig. 8 h. The differences in these colors can be seen between the buffer and the composite gel, suggesting that the thermosensitive POEA is decomposed by the heat generated via these Fe-Si nanoparticles and the dye releases.

Magnetic resonance imaging

For elements that contain an odd number of protons and neutrons, they exhibit intrinsic magnetic moments that are the primary origin of the MRI signals. In MRI applications, the magnetic resonance signals mainly come from the protons, which is abundant in water and lipid molecules. MNPs have been used as contrast agents in MRI applications where the MNP provides inherent signal amplification and affects billions of adjacent water protons.

Magnetic materials with high saturation magnetization are desired for MRI applications. Besides FeCo alloys, some Fe_xN_{1-x} also have high saturation magnetization such as γ'-Fe_4N and α"-$Fe_{16}N_2$. The saturation magnetization of α"-$Fe_{16}N_2$ is up to 2300 emu/cm^3 (Kim and Takahashi 1972; Sugita et al. 1991; Ji et al.

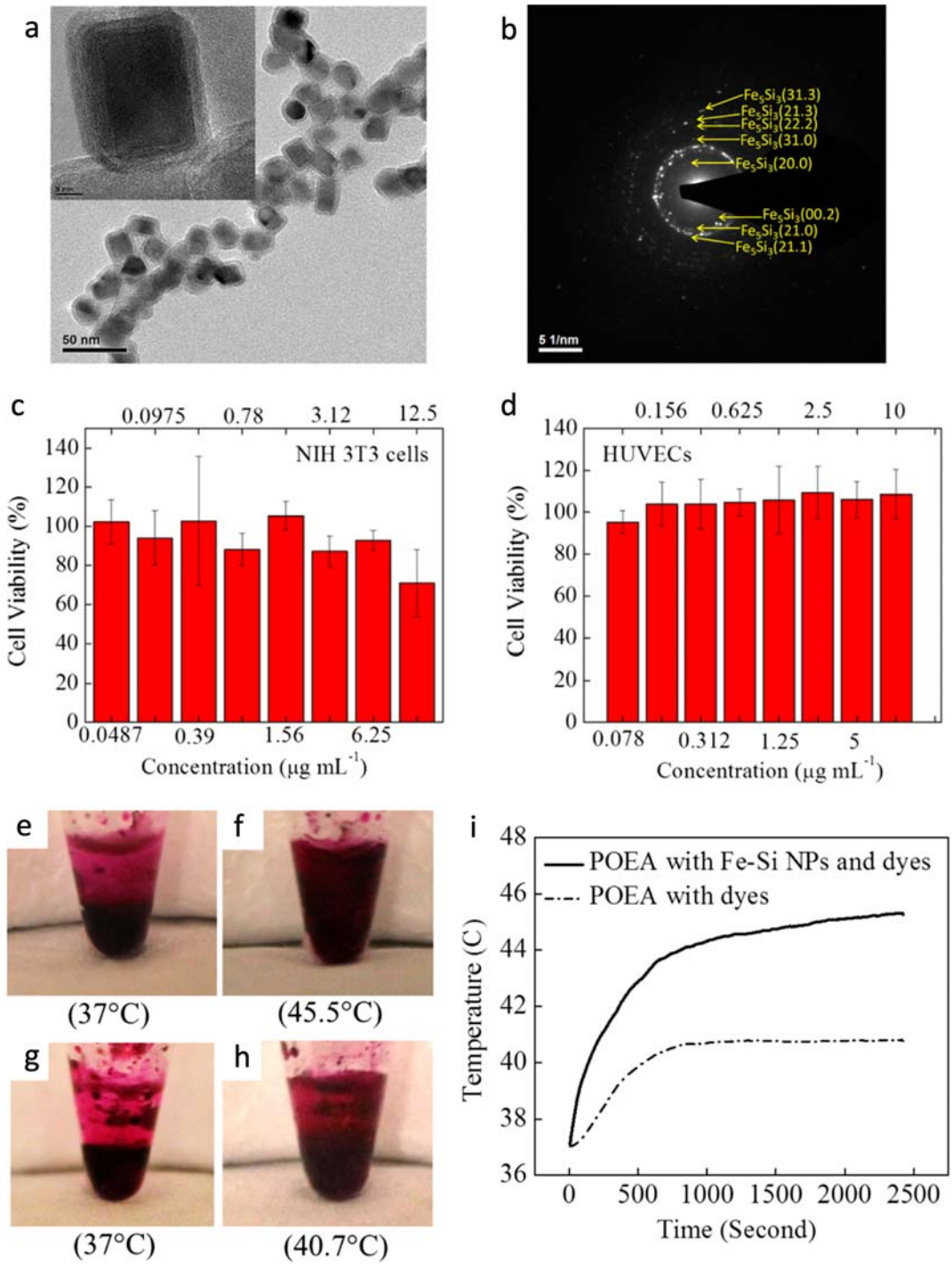

Fig. 8 **a** Bright-field TEM image of Fe-Si nanoparticles. **b** SAD of Fe-Si NPs. **c** Viability of mouse embryonic fibroblasts (NIH 3 T3) after treatment with Fe-Si NPs at different concentrations. **d** Cytotoxicity result of Fe-Si NPs on HUVECs. **e–i** Dye release under magnetic field heating by POEA/Fe-Si NPs composite. Photos of POEA copolymer loaded with Fe-Si NPs and dyes **e** before applying the magnetic field at 37 °C and **f** after applying the magnetic field. Photos of POEA copolymer loaded with dyes **g** before applying the magnetic field at 37 °C and **h** after applying the magnetic field. **i** Temperature rise versus time for POEA copolymer loaded with Fe-Si NPs and dyes and POEA copolymer loaded with dyes only. (reprinted with permission from Jing et al. (2015), copyright 2015 American Chemical Society)

2011; Wang et al. 2012), which is even larger than that of FeCo alloys. The high saturation magnetization makes this material a promising candidate for potential bio-applications. Even for γ'-Fe_4N, its specific saturation magnetization is reported 182 emu/g that is much higher than that of iron oxide MNPs (70~80 emu/g) (Wu et al. 2004). Wu et al. reported that irregularly shaped γ'-Fe_4N MNPs for hyperthermia treatment and T2 contrast-enhanced MRI (Wu et al. 2019a). The irregular shape and high saturation magnetization of γ'-Fe_4N MNPs can induce inhomogeneous distribution of magnetic field, which is the significant advantage for MRI applications. The inhomogeneity could vary the relaxation times at a specific region to be imaged. Thus, the contrast efficiency between adjacent tissue for MRI could be improved.

Another high-moment material is FeCo alloys. However, core-shell structure FeCo MNPs are preferred due to the concerns of easy oxidation and potential toxicity (Hütten et al. 2004; Reiss and Hütten 2005). FeCo core-shell MNPs with shell materials such as graphitic carbon, pyrolytic carbon, silica, or inert metals are reported (Bai et al. 2007a; Abbas et al. 2015; Yang et al. 2017; Gao 2018). In 2010, Patra et al. reported a FeCo@Au core-shell structure MNPs for the therapeutic and diagnostic application of angiogenesis-dependent disorders but also for the monitoring of the treatment on the disease outcome (Patra et al. 2010).

FeCo@Au MNPs are used as contrast agents in MRI, where the Au shell inhibits the function of a pro-angiogenic growth factor. VEGF165 (vascular endothelial growth factor 165), and the self-contrast property of FeCo@Au, is determined in vitro by MRI (Patra et al. 2010). In 2006, Seo et al. firstly reported the FeCo-graphitic carbon (FeCo-GC) core-shell nanocrystals as MRI and near-infrared (NIR) agents (Seo et al. 2006). The multiple functionalities of these core-shell materials are explored by characterizing the magnetic properties of the FeCo core and the near-infrared optical absorbance of the graphitic shell. The FeCo-GC nanocrystals show ultra-high saturation magnetization, r1 and r2 relaxivities, and high optical absorbance in the near-infrared region. It points out the possibility of using these nanocrystals for integrated diagnosis and therapeutic applications. Later in 2011, Sherlock et al. reported the multifunctional FeCo-graphitic carbon (FeCo-GC) core-shell nanocrystals (4–5 nm in diameter) for combined drug delivery, near-infrared (NIR) photothermal therapy, and MRI (Sherlock et al. 2011; Sherlock and Dai 2011). With the graphitic shell, these nanocrystals show the high-efficiency loading of doxorubicin (DOX) and pH-sensitive DOX release abilities. They observed enhanced intracellular drug delivery by FeCo/GC-DOX under 20 min of NIR laser (808 nm) induced hyperthermia to 43 °C, resulting in a significant increase of FeCo/GC-DOX toxicity toward breast cancer cells. That is due to the twofold enhancement of cancer cell uptake of FeCo/GC-DOX complexes and the increased DOX toxicity under the 43 °C hyperthermia condition. While this FeCo/GC-DOX system is evaluated in vitro, it could be readily translated to an in vivo treatment method.

Takahashi et al. reported the design of Ag-FeCo-Ag core-shell nanoparticles for magnetic separation of subcellular components like intracellular vesicles (Takahashi et al. 2015). Furthermore, the Ag layer allows plasmon scattering. Thus, these nanoparticles are considered as a potential alternative to existing fluorescent probes like dye molecules and colloidal quantum dots.

Furthermore, a recent emerging technique, magnetic particle imaging (MPI), is also questing after the high-moment superparamagnetic nanoparticles for the best imaging performance (Du et al. 2013; Wu et al. 2019c). The high-moment FeCo MNPs combined with a proper surface coating layer could potentially take over iron oxide MNPs. In magnetic nanoparticle spectroscopy-based bioassays, the single-core, superparamagnetic nanoparticles are of great interest for researchers due to the strong magnetic responses to the alternating magnetic field.

Besides the aforementioned biomedical applications, high-moment MNPs have also been exploited for other applications. There have been many research works reporting that the FeCo@graphene, FeCo@SiO_2, FeCo@SnO_2, FeCo@$CoFe_2O_4$, FeCo@C nanoparticles/nanotubes/nanoplates/nanoflakes show enhanced electromagnetic wave absorption properties and could be used as efficient broadband electromagnetic wave absorber (Wang et al. 2016, 2017; Li et al. 2019).

Application on GMR biosensors

High-moment MNPs as magnetic tags for biomarkers

Superparamagnetic MNPs with high saturation magnetization have been widely employed as the magnetic tags for giant magnetoresistance (GMR) sensor-based biomarker detection Su et al. (2020). After the biofunctionalization of a GMR sensor, the target biomarkers can bound to the

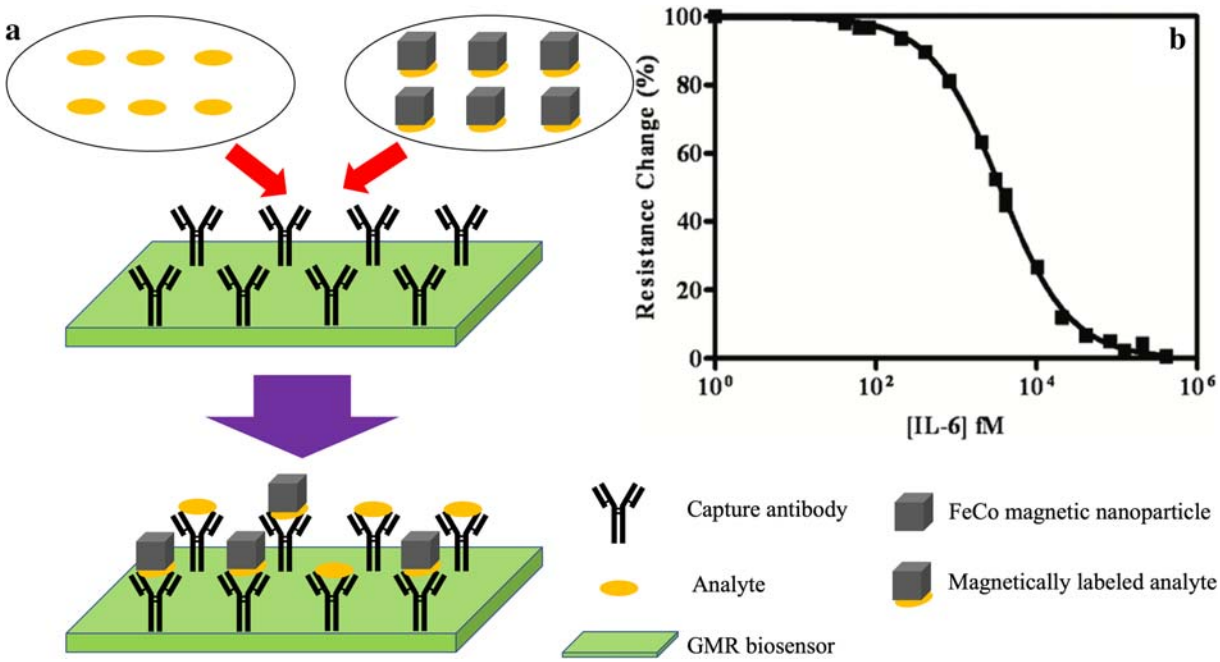

Fig. 9 **a** Competition-based two-layer detection scheme: the IL-6 molecules with and without MNP tags compete for binding sites on the sensor surface. **b** The response curve of the competition-based assay with varying concentrations of unlabeled IL-6 molecules (Reprinted with permission from(Li et al. 2010), copyright 2010 American Chemical Society)

sensor surface via either antibody-antigen reaction or the reaction between two complementary DNA strands. The surface-functionalized high-moment MNPs can then bound to the target biomarkers on the GMR sensor surface. After the application of an external magnetic field, the stray fields generated by these bounded MNPs can be detected by the GMR sensors underneath, as shown in Fig. 9. For higher concentrations of biomarkers, there will be more MNPs near the sensor surface, which will result in the larger stray field and the hence larger sensor signal. A larger stray field generated per MNP is required to improve the sensitivity of the biomarker detection, which makes high-moment MNPs promising candidates for magnetic tags.

The detection of human interleukin (IL-6), a potential lung cancer biomarker with high-moment FeCo MNPs and GMR sensors, was demonstrated by Srinivasan et al. (2009b). The FeCo MNPs were synthesized by the previously mentioned GPC technique. The synthesized MNPs were cubic, with an average size of 12.8 nm in diameter. The net magnetic moment per particle is 1.77×10^{-17} emu, which is more than eight times higher than the γ-Fe_2O_3 nanoparticle of the same size under an external field of 100 Oe. The FeCo nanoparticles are functionalized with streptavidin to facilitate the subsequent binding process. GMR sensors with a structure of Ta (5 nm)/$Ir_{0.8}Mn_{0.2}$ (10 nm)/$Co_{0.9}Fe_{0.1}$ (2.5 nm)/Cu (3.3 nm)/$Co_{0.9}Fe_{0.1}$ (1 nm)/$Ni_{0.82}Fe_{0.12}$ (2 nm)/Ta (5 nm) are deposited by a magnetron sputtering system. Different amounts of the streptavidin-coated MNPs are added to the biotin-functionalized GMR sensor to determine the dynamic range of the sensing system. It was found that the range of linearity for the detection of streptavidin was from 600 copies to more than 20,000 copies with the limit of detection (LOD) in the zeptomole range. The sensing system was then validated through the detection of human IL-6 by building up a capture antibody biomarker detection antibody MNP sandwich structure on the sensor surface. A similar linear response curve was observed for different concentrations of IL-6 molecules with a LOD of 2.08×10^6 molecules.

A year later, Li et al. reported the detection of the same biomarker with improved sensitivity via the application of a two-layer detection scheme (Li et al. 2010). Despite the similar GMR sensor structures, the magnetic immunoassay utilizes a two-layer structure instead of the traditional three-layer structure. In this paper, the target analytes are directly bound to the FeCo MNPs without any detection antibodies. It was found that the

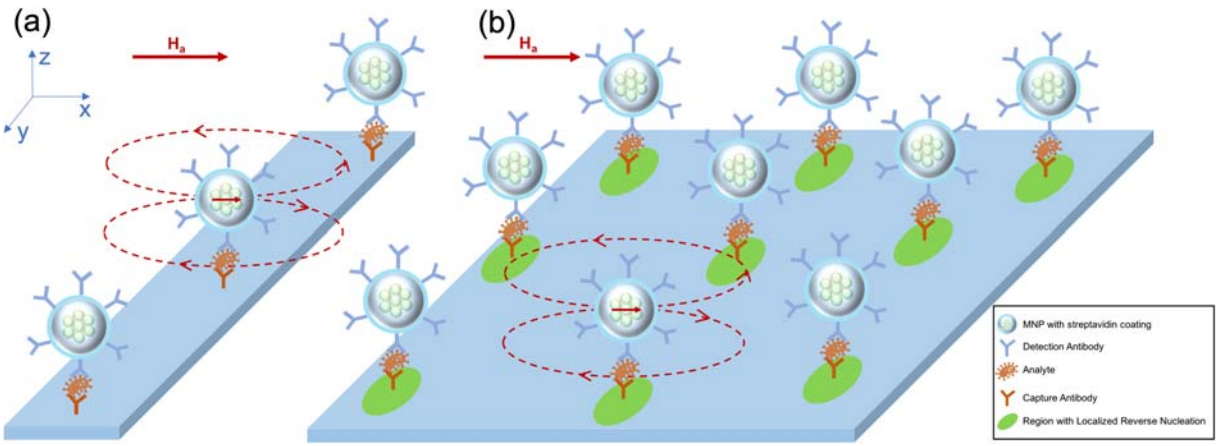

Fig. 10 Schematic illustration of the detection process of **a** stripe-shaped sensors with high aspect ratio; **b** large-area GMR sensors with localized nucleation sites under each MNP. (Reprinted with permission from Su et al. (2019b), copyright 2019 Elsevier)

LOD of the two-layer approach reached 373 fM, which was 55 times more sensitive than the 3-layer approach. A competition-based two-layer approach was further developed where a certain concentration of magnetically labeled analyte was mixed with varying concentrations of an unlabeled analyte to compete for the binding sites, as shown in Fig. 9. It was shown that with this assay, the detection of human IL-6 with GMR sensors and high-moment MNPs could also be performed in unprocessed human urine with superior sensitivity compared to the enzyme-linked immunosorbent assays (ELISA). Besides the human IL-6, other biomarkers such as endoglin (Srinivasan et al. 2011), which is the biomarker for prostate cancer, have also been successfully detected and quantified by the high-moment MNPs integrated with GMR sensors. That provides a promising approach toward the early and rapid biological detection.

Exploring novel sensing mechanisms with high-moment MNPs

The GMR stacks are often fabricated into stripe-shaped devices with high aspect ratios to increase the linearity and sensitivity of the GMR biosensors (Krishna et al. 2016; Choi et al. 2016; Wu et al. 2017; Su et al. 2019a). However, in biological applications, the reduced sensor width can also lead to a decreased sensing area and increased Johnson noise due to the larger sensor resistance. Furthermore, the sensor signal can also vary with the position of the MNPs relative to the edges of the sensing elements (Klein et al. 2014). An alternative approach is the application of GMR sensors with low aspect ratios. Feng et al. explored the possibility of magnetic reversal nucleation-based switching induced by high-moment MNPs in large-area GMR sensors (Feng et al. 2017). The dipole field from the MNPs can form localized nucleation sites inside the sensor, which will assist the magnetization reversal and thus produce sensor signals that are proportional to the number of MNPs.

To evaluate the influence of high-moment MNPs on the switching of GMR sensors, FeCo MNPs were deposited onto a GMR sensor surface with the GMR transfer curves measured before and after the deposition. A significant shift in the transfer curve was observed, which was attributed to the decreased nucleation field resulting from the reduced local magnetic anisotropy due to the stray field of FeCo MNPs. Su et al. simulated the magnetization reversal process in permalloy thin films through the Object Oriented Micromagnetic Framework (OOMMF) (Su et al. 2019b). FeCo MNPs with diameters of 10 nm were put on top of a 4 $\mu m \times$ 4 μm permalloy thin film. It was found that a reverse nucleation site was generated under each FeCo MNP, as shown in Fig. 10. Since the direction of the stray field from FeCo MNPs was always opposite to the direction of the applied magnetic field, the existence of the MNPs can either assist or prevent the switching process, leading to a shift in the transfer curves. The magnetoresistance changes in both types of sensors with various MNP concentrations were calculated to compare the performance of large-area sensors with stripe-shaped sensors. The sensitivity of the large-area GMR sensors was found to be 20 times larger than that of the stripe-shaped sensors, which demonstrated the superior performance of large-area GMR sensors with high-moment MNPs as tags in the field of biomarker detection.

Conclusions

Driven by the various applications, high-moment MNPs are highly demanded. In this paper, we summarized the sputtering-based GPC method used for preparing high-moment MNPs. The mechanisms of the GPC method to fabricate MNPs were investigated. The field-controlled plasma heating effect is the key to making MNPs with good crystallinity. Magnetic field distribution near the target surface was tuned by a soft iron ring and cone, which in turn adjusted the plasma heating effect. Based on this effect, several kinds of high-moment MNPs with different phases were reported. In addition, core-shell MNPs were successfully fabricated to make the high-moment MNPs biocompatible. The high-moment MNPs were used in several bio-applications such as magnetic hyperthermia, drug delivery, MRI, and GMR-based biosensors. It is manifested that high-moment MNPs prepared by the GPC system are promising candidates for bio-applications.

Funding information This study was financially supported by the Institute of Engineering in Medicine of the University of Minnesota through FY18 IEM Seed Grant Funding Program, the National Science Foundation MRSEC facility program, the Distinguished McKnight University Professorship, the Centennial Chair Professorship, and the Robert F Hartmann Endowed Chair from the University of Minnesota. Parts of this work were carried out in the Characterization Facility, University of Minnesota, which receives partial support from NSF through the MRSEC program.

Compliance with ethical standards

Conflict of interest The authors declare that they have no conflict of interest.

References

Abbas M, Islam MN, Rao BP et al (2015) Facile approach for synthesis of high moment Fe/ferrite and FeCo/ferrite core/shell nanostructures. Mater Lett 139:161–164. https://doi.org/10.1016/j.matlet.2014.10.078

Bai J, Wang J-P (2005) High-magnetic-moment core-shell-type FeCo–au Ag nanoparticles. Appl Phys Lett 87:152502. https://doi.org/10.1063/1.2089171

Bai J, Xu Y-H, Thomas J, Wang J-P (2007a) (FeCo) 3 Si–SiO x core–shell nanoparticles fabricated in the gas phase. Nanotechnology 18:065701. https://doi.org/10.1088/0957-4484/18/6/065701

Bai J, Xu Y, Wang J (2007b) Cubic and spherical high-moment FeCo nanoparticles with narrow size distribution. IEEE Trans Magn 43:3340–3342. https://doi.org/10.1109/TMAG.2007.893781

Bañobre-López M, Teijeiro A, Rivas J (2013) Magnetic nanoparticle-based hyperthermia for cancer treatment. Rep Pract Oncol Radiother 18:397–400. https://doi.org/10.1016/j.rpor.2013.09.011

Bárcena C, Sra AK, Gao J (2009) Applications of magnetic nanoparticles in biomedicine. In: Nanoscale magnetic materials and applications. Springer US, Boston, MA, pp 591–626

Bulut F, Rosellen W, Getzlaff M (2009) Structural properties of size-selected FeCo nanoparticles deposited on W(110). Appl Phys A Mater Sci Process 97:185–189. https://doi.org/10.1007/s00339-009-5230-2

Çelik Ö, Fırat T (2018) Synthesis of FeCo magnetic nanoalloys and investigation of heating properties for magnetic fluid hyperthermia. J Magn Magn Mater 456:11–16. https://doi.org/10.1016/j.jmmm.2018.01.090

Choi J, Gani AW, Bechstein DJB et al (2016) Portable, one-step, and rapid GMR biosensor platform with smartphone interface. Biosens Bioelectron 85:1–7. https://doi.org/10.1016/j.bios.2016.04.046

Dobson J (2006) Magnetic nanoparticles for drug delivery. Drug Dev Res 67:55–60. https://doi.org/10.1002/ddr.20067

Du Y, Lai P, Leung C, Pong P (2013) Design of superparamagnetic nanoparticles for magnetic particle imaging (MPI). Int J Mol Sci 14:18682–18710. https://doi.org/10.3390/ijms140918682

Feng Y, Liu J, Klein T et al (2017) Localized detection of reversal nucleation generated by high moment magnetic nanoparticles using a large-area magnetic sensor. J Appl Phys 122:123901. https://doi.org/10.1063/1.5001919

Gao Y (2018) Carbon nano-allotrope/magnetic nanoparticle hybrid nanomaterials as T2 contrast agents for magnetic resonance imaging applications. J Funct Biomater 9:16. https://doi.org/10.3390/jfb9010016

Granqvist CG (1976) Ultrafine metal particles. J Appl Phys 47:2200. https://doi.org/10.1063/1.322870

Haberland H, Karrais M, Mall M (1991) A new type of cluster and cluster ion source. Atoms Mol Clust 20:413–415. https://doi.org/10.1007/BF01544025

Haberland H, Martin K, Martin M, Yonca T (1992) Thin films from energetic cluster impact: a feasibility study. J Vac Sci Technol A 10:3266–3271. https://doi.org/10.1116/1.577853

He S, Jing Y, Wang J-P (2013) Direct synthesis of large size ferromagnetic SmCo5 nanoparticles by a gas-phase condensation method. J Appl Phys 113:134310. https://doi.org/10.1063/1.4798475

Hedayatnasab Z, Abnisa F, Daud WMAW (2017) Review on magnetic nanoparticles for magnetic nanofluid hyperthermia application. Mater Des 123:174–196. https://doi.org/10.1016/j.matdes.2017.03.036

Hergt R, Hiergeist R, Hilger I et al (2004) Maghemite nanoparticles with very high AC-losses for application in RF-magnetic hyperthermia. J Magn Magn Mater 270:345–357. https://doi.org/10.1016/j.jmmm.2003.09.001

Hu M-J, Lu Y, Zhang S, Guo SR, Lin B, Zhang M, Yu SH (2008) High yield synthesis of bracelet-like hydrophilic Ni-Co magnetic alloy flux-closure nanorings. J Am Chem Soc 130:11606–11607. https://doi.org/10.1021/ja804467g

Hütten A, Sudfeld D, Ennen I, Reiss G, Hachmann W, Heinzmann U, Wojczykowski K, Jutzi P, Saikaly W, Thomas G (2004)

New magnetic nanoparticles for biotechnology. J Biotechnol 112:47–63. https://doi.org/10.1016/j.jbiotec.2004.04.019

Ji N, Allard LF, Lara-Curzio E, Wang J-P (2011) N site ordering effect on partially ordered Fe[sub 16]N[sub 2]. Appl Phys Lett 98:092506. https://doi.org/10.1063/1.3560051

Jian-Ping Wang (2008) FePt magnetic nanoparticles and their assembly for future magnetic media. Proc IEEE 96:1847–1863. https://doi.org/10.1109/JPROC.2008.2004318

Jing Y, Sohn H, Kline T et al (2009) Experimental and theoretical investigation of cubic FeCo nanoparticles for magnetic hyperthermia. J Appl Phys 105:07B305. https://doi.org/10.1063/1.3074136

Jing Y, He SH, Wang JP (2013) Composition-and phase-controlled high-magnetic-moment Fe 1-xCox nanoparticles for biomedical applications. IEEE Trans Magn 49:197–200. https://doi.org/10.1109/TMAG.2012.2226236

Jing Y, Liu J, Ji W-H, Wang W, He SH, Jiang XZ, Wiedmann T, Wang C, Wang JP (2015) Biocompatible Fe–Si nanoparticles with adjustable self-regulation of temperature for medical applications. ACS Appl Mater Interfaces 7:12649–12654. https://doi.org/10.1021/acsami.5b01680

Kim TK, Takahashi M (1972) New magnetic material having ultrahigh magnetic moment. Appl Phys Lett 20:492–494. https://doi.org/10.1063/1.1654030

Klein T, Wang Y, Tu L et al (2014) Comparative analysis of several GMR strip sensor configurations for biological applications. Sensors Actuators A Phys 216:349–354. https://doi.org/10.1016/j.sna.2014.05.033

Kline TL, Xu YH, Jing Y, Wang JP (2009) Biocompatible high-moment FeCo-au magnetic nanoparticles for magnetic hyperthermia treatment optimization. J Magn Magn Mater 321:1525–1528. https://doi.org/10.1016/j.jmmm.2009.02.079

Krishna VD, Wu K, Perez AM, Wang J-P (2016) Giant Magnetoresistance-based biosensor for detection of influenza a virus. Front Microbiol 7:1–8. https://doi.org/10.3389/fmicb.2016.00400

Krishna VD, Wu K, Su D et al (2018) Nanotechnology: review of concepts and potential application of sensing platforms in food safety. Food Microbiol 75:47–54. https://doi.org/10.1016/j.fm.2018.01.025

Lacroix L-M, Malaki RB, Carrey J et al (2009) Magnetic hyperthermia in single-domain monodisperse FeCo nanoparticles: evidences for Stoner–Wohlfarth behavior and large losses. J Appl Phys 105:023911. https://doi.org/10.1063/1.3068195

Li Y, Jing Y, Yao X et al (2009) Biomarkers identification and detection based on GMR sensor and sub 13 nm magnetic nanoparticles. In: 2009 annual international conference of the IEEE engineering in medicine and biology society. IEEE, pp 5432–5435

Li Y, Srinivasan B, Jing Y, Yao X, Hugger MA, Wang JP, Xing C (2010) Nanomagnetic competition assay for low-abundance protein biomarker quantification in unprocessed human sera. J Am Chem Soc 132:4388–4392. https://doi.org/10.1021/ja910406a

Li S, Huang Y, Zhang N et al (2019) Synthesis of polypyrrole decorated FeCo@SiO2 as a high-performance electromagnetic absorption material. J Alloys Compd 774:532–539. https://doi.org/10.1016/j.jallcom.2018.09.349

Liu J, Wu K, Wang J-P (2016) Magnetic properties of cubic FeCo nanoparticles with anisotropic long chain structure. AIP Adv 6:056126. https://doi.org/10.1063/1.4945042

Liu J, Schliep K, He SH et al (2018) Iron nanoparticles with tunable tetragonal structure and magnetic properties. Phys Rev Mater 2:054415. https://doi.org/10.1103/PhysRevMaterials.2.054415

Liu J, He S, Wang J-P (2019a to be submitted) A gas-condensation system with a hollow cathode for synthesizing magnetic nanoparticles with high yield

Liu J, Guo G, Zhang F et al (2019b) Synthesis of α″-Fe 16 N 2 ribbons with a porous structure. Nanoscale Adv 1:1337–1342. https://doi.org/10.1039/C9NA00008A

Liu J, Guo G, Zhang X et al (2020a) Synthesis of α″-Fe16N2 foils with an ultralow temperature coefficient of coercivity for rare-earth-free magnets. Acta Mater 184:143–150. https://doi.org/10.1016/j.actamat.2019.11.052

Liu J, Zhang D, Wu K et al (2020b) Magnetic field enhanced coercivity of Fe nanoparticles embedded in antiferromagnetic MnN films. J Phys D Appl Phys 53:035003. https://doi.org/10.1088/1361-6463/ab4c58

Ong PL, Mahmood S, Zhang T et al (2008) Synthesis of FeCo nanoparticles by pulsed laser deposition in a diffusion cloud chamber. Appl Surf Sci 254:1909–1914. https://doi.org/10.1016/j.apsusc.2007.07.186

Patra CR, Jing Y, Xu YH, Bhattacharya R, Mukhopadhyay D, Glockner JF, Wang JP, Mukherjee P (2010) A core-shell nanomaterial with endogenous therapeutic and diagnostic functions. Cancer Nanotechnol 1:13–18. https://doi.org/10.1007/s12645-010-0002-4

Qiu J-M, Wang J-P (2006) Monodispersed and highly ordered L1[sub 0] FePt nanoparticles prepared in the gas phase. Appl Phys Lett 88:192505. https://doi.org/10.1063/1.2202130

Qiu J-M, Wang J-P (2007) Tuning the crystal structure and magnetic properties of FePt nanomagnets. Adv Mater 19:1703–1706. https://doi.org/10.1002/adma.200602374

Qiu J-M, Judy JH, Weller D, Wang J-P (2005) Toward the direct deposition of L10 FePt nanoparticles. J Appl Phys 97:10J319. https://doi.org/10.1063/1.1855211

Reiss G, Hütten A (2005) Magnetic nanoparticles: applications beyond data storage. Nat Mater 4:725–726. https://doi.org/10.1038/nmat1494

Sattler K, Mühlbach J, Recknagel E (1980) Generation of metal clusters containing from 2 to 500 atoms. Phys Rev Lett 45:821–824. https://doi.org/10.1103/PhysRevLett.45.821

Seo WS, Lee JH, Sun X, Suzuki Y, Mann D, Liu Z, Terashima M, Yang PC, McConnell M, Nishimura DG, Dai H (2006) FeCo/graphitic-shell nanocrystals as advanced magnetic-resonance-imaging and near-infrared agents. Nat Mater 5:971–976. https://doi.org/10.1038/nmat1775

Serkova NJ (2017) Nanoparticle-based magnetic resonance imaging on tumor-associated macrophages and inflammation. Front Immunol 8:590. https://doi.org/10.3389/fimmu.2017.00590

Sherlock SP, Dai H (2011) Multifunctional FeCo-graphitic carbon nanocrystals for combined imaging, drug delivery and tumor-specific photothermal therapy in mice. Nano Res 4:1248–1260. https://doi.org/10.1007/s12274-011-0176-z

Sherlock SP, Tabakman SM, Xie L, Dai H (2011) Photothermally enhanced drug delivery by ultrasmall multifunctional FeCo/graphitic shell nanocrystals. ACS Nano 5:1505–1512. https://doi.org/10.1021/nn103415x

Srinivasan B, Li Y, Jing Y et al (2009a) A detection system based on giant magnetoresistive sensors and high-moment

magnetic nanoparticles demonstrates zeptomole sensitivity: potential for personalized medicine. Angew Chem 121: 2802–2805. https://doi.org/10.1002/ange.200806266

Srinivasan B, Li Y, Jing Y et al (2009b) A detection system based on giant magnetoresistive sensors and high-moment magnetic nanoparticles demonstrates zeptomole sensitivity: potential for personalized medicine. Angew Chem Int Ed 48:2764–2767. https://doi.org/10.1002/anie.200806266

Srinivasan B, Li Y, Jing Y, Xing C, Slaton J, Wang JP (2011) A three-layer competition-based giant magnetoresistive assay for direct quantification of endoglin from human urine. Anal Chem 83:2996–3002. https://doi.org/10.1021/ac2005229

Su et al (2020), Advances in Magnetoresistive Biosensors, Micromachines, 1:34. https://doi.org/10.3390/mi11010034

Su D, Wu K, Krishna VD et al (2019a) Detection of influenza a virus in swine nasal swab samples with a wash-free magnetic bioassay and a handheld giant magnetoresistance sensing system. Front Microbiol 10:1–10. https://doi.org/10.3389/fmicb.2019.01077

Su D, Wu K, Wang J-P (2019b) Large-area GMR bio-sensors based on reverse nucleation switching mechanism. J Magn Magn Mater 473:484–489. https://doi.org/10.1016/j.jmmm.2018.10.112

Sugimoto T (1987) Preparation of monodispersed colloidal particles. Adv Colloid Interface 28:65–108

Sugita Y, Mitsuoka K, Komuro M et al (1991) Giant magnetic moment and other magnetic properties of epitaxially grown Fe16N2 single-crystal films (invited). 70:5977–5982

Takahashi M, Mohan P, Nakade A, Higashimine K, Mott D, Hamada T, Matsumura K, Taguchi T, Maenosono S (2015) Ag/FeCo/Ag Core/Shell/Shell magnetic nanoparticles with plasmonic imaging capability. Langmuir 31:2228–2236. https://doi.org/10.1021/la5046805

Wang J-P (2019) Environment-friendly bulk Fe16N2 permanent magnet: review and prospective. J Magn Magn Mater 165962. https://doi.org/10.1016/j.jmmm.2019.165962

Wang J-P, Qiu J-M, Taton TA, Kim B-S (2006) Direct preparation of highly ordered$rm L10 phase FePt nanoparticles and their shape-assisted assembly. IEEE Trans Magn 42:3042–3047. https://doi.org/10.1109/TMAG.2006.880150

Wang JP, Ji N, Liu X, et al (2012) Fabrication of Fe16N2films by sputtering process and experimental investigation of origin of giant saturation magnetization in Fe16N2. In: IEEE Transactions on Magnetics. pp 1710–1717

Wang Y, Zhang W, Luo C et al (2016) Superparamagnetic FeCo@SnO 2 nanoparticles on graphene-polyaniline: synthesis and enhanced electromagnetic wave absorption properties. Ceram Int 42:12496–12502. https://doi.org/10.1016/j.ceramint.2016.05.038

Wang Y, Wu X, Zhang W et al (2017) Synthesis of ferromagnetic sandwich FeCo@graphene@PPy and enhanced electromagnetic wave absorption properties. J Magn Magn Mater 443: 358–365. https://doi.org/10.1016/j.jmmm.2017.07.063

Wei X-W, Zhu G-X, Liu Y-J et al (2008) Large-scale controlled synthesis of FeCo nanocubes and microcages by wet chemistry. Chem Mater 20:6248–6253. https://doi.org/10.1021/cm800518x

Wu K, Wang J-P (2017) Magnetic hyperthermia performance of magnetite nanoparticle assemblies under different driving fields. AIP Adv 7:056327. https://doi.org/10.1063/1.4978458

Wu XL, Zhong W, Jiang HY et al (2004) Magnetic properties and thermal stability of γ′-Fe4N nanoparticles prepared by a combined method of reduction and nitriding. J Magn Magn Mater 281:77–81. https://doi.org/10.1016/j.jmmm.2004.03.043

Wu K, Klein T, Krishna VD et al (2017) Portable GMR handheld platform for the detection of influenza a virus. ACS Sensors 2:1594–1601. https://doi.org/10.1021/acssensors.7b00432

Wu K, Liu J, Saha R et al (2019a) Irregularly shaped γ'-Fe4N nanoparticles for hyperthermia treatment and T2 contrast-enhanced magnetic resonance imaging with minimum dose

Wu K, Su D, Liu J, Saha R, Wang JP (2019b) Magnetic nanoparticles in nanomedicine: a review of recent advances. Nanotechnology 30:502003. https://doi.org/10.1088/1361-6528/ab4241

Wu K, Su D, Saha R et al (2019c) Magnetic particle spectroscopy-based bioassays: methods, applications, advances, and future opportunities. J Phys D Appl Phys 52:173001. https://doi.org/10.1088/1361-6463/ab03c0

Xu Y (2007) Direct synthesis of multifunctional heterostructured magnetic nanoparticles in gas phase

Xu Y, Wang J (2007) FeCo–au core-shell nanocrystals. Appl Phys Lett 91:233107. https://doi.org/10.1063/1.2823574

Xu Y-H, Wang J-P (2008) Direct gas-phase synthesis of heterostructured nanoparticles through phase separation and surface segregation. Adv Mater 20:994–999. https://doi.org/10.1002/adma.200602895

Xu YH, Bai J, Wang J-P (2007) High-magnetic-moment multifunctional nanoparticles for nanomedicine applications. J Magn Magn Mater 311:131–134. https://doi.org/10.1016/j.jmmm.2006.11.174

Xu C, Yuan Z, Kohler N, Kim J, Chung MA, Sun S (2009) FePt nanoparticles as an Fe reservoir for controlled Fe release and tumor inhibition. J Am Chem Soc 131:15346–15351

Yamamuro S, Sumiyama K, Sakurai M, Suzuki K (1998) Cr cluster deposition by plasma—gas-condensation method. Supramol Sci 5:239–245. https://doi.org/10.1016/S0968-5677(98)00014-5

Yamamuro S, Sumiyama K, Suzuki K (1999) Monodispersed Cr cluster formation by plasma-gas-condensation. J Appl Phys 85:483–489. https://doi.org/10.1063/1.369476

Yang F, Chen H, Liu D et al (2017) The microstructure and magnetic properties of FeCo@SiO2 core-shell nanoparticles synthesized by using a solution method. J Alloys Compd 728:1153–1156. https://doi.org/10.1016/j.jallcom.2017.09.126

Yu L, Liu J, Wu K, Klein T, Jiang Y, Wang JP (2014) Evaluation of hyperthermia of magnetic nanoparticles by dehydrating DNA. Sci Rep 4:7216. https://doi.org/10.1038/srep07216

Zeisberger M, Dutz S, Müller R et al (2007) Metallic cobalt nanoparticles for heating applications. J Magn Magn Mater 311:224–227. https://doi.org/10.1016/j.jmmm.2006.11.178

Zhang L, Gu F, Chan J, Wang AZ, Langer RS, Farokhzad OC (2008) Nanoparticles in medicine: therapeutic applications and developments. Clin Pharmacol Ther 83:761–769. https://doi.org/10.1038/sj.clpt.6100400